Received: 16 April 2020 | Revised: 27 July 2021 | Accepted: 30 July 2021
DOI: 10.1002/gj.4236

RESEARCH ARTICLE

WILEY

Geochronology and tectonic significance of A-type granite from Misho, NW Iran: Implications for the detachment of Cimmeria from Gondwana and the opening of Neo-Tethys

Susan Jamei[1,2] | **Mansour Ghorbani**[1] | **Amin Jafari**[2,3] | **Ian S. Williams**[2] | **Mohsen Moayyed**[3]

[1]Faculty of Earth Sciences, Shahid Beheshti University, Tehran, Iran

[2]Research School of Earth Sciences, Australian National University, Canberra, Australia

[3]Department of Earth Sciences, Faculty of Natural Sciences, University of Tabriz, Tabriz, Iran

Correspondence
Susan Jamei, Faculty of Earth Sciences, Shahid Beheshti University, Tehran, Iran.
Email: s_jamei@sbu.ac.ir

Handling Editor: E. Bozkurt

The Cimmerian Terrane, part of which forms the Central Iranian Plateau, is one of several continental fragments produced during the early- to mid-Palaeozoic breakup of the northern margin of Gondwana. Magmatic evidence for the final separation of the Terrane from Gondwana and formation of the intervening Neo-Tethys Ocean is preserved in the Misho Mountains SW of Marand, NW Iran. A small (30 km^2) body of subalkaline granite intruding Precambrian sedimentary rocks of the Kahar Formation has numerous chemical features that identify it as an A-type granite, including high Ga/Al, $K_2O + Na_2O$, $FeO_t/(FeO_t + MgO)$ and incompatible elements (LILE and HFSE), and low CaO and P_2O_5. Such features are consistent with the asthenospheric upwelling above a rising mantle plume. Zircon ages of 350.8 ± 3.0, 345.4 ± 3.2, and 343.6 ± 4.0 Ma measured on three samples of the Misho A-type granite along with the same granites exposed in the western domain (Herris area, ~306 Ma) reveal that the crystallization process occurred sequentially in different stages. The obtained ages record detachment of the Cimmerian Terrane from Gondwana and the initiation of Neo-Tethys at least in the Early Carboniferous, significantly earlier than previous researchers have proposed.

KEYWORDS
Cimmeria, Gondwana, Iran, Misho A-type granite, Neo-Tethys

1 | INTRODUCTION

Although the assembly of Gondwana has received increasing attention over recent decades, the break-up of the supercontinent remains a matter of debate. In particular, the recognition of a number of continental fragments formerly belonging to northern Gondwana raises the question of whether they separated from the supercontinent at different times, forming different branches of ancient oceans with different tectonic histories. The break-up of Gondwana in the vicinity of modern Iran produced two ocean basins, Palaeo- and Neo-Tethys. Major pre-Permian sequences (Figure 1), palaeomagnetic, and geochronological data, as well as palaeobiogeographic evidence from Iran and Gondwana, show that Iran was part of the Gondwanan landmass until at least the earliest Carboniferous (e.g., Arefifard, 2017; Jamei, Ghorbani, Williams, & Moayyed, 2020; Muttoni et al., 2009; Soffel & Forster, 1980), after which it separated by Neo-Tethys opening from the supercontinent as part of the Cimmerian Terrane and moved northwards towards Eurasia (Figure 2). Various reconstructions of the tectonic configuration during the detachment of the Iranian Cimmeria have been proposed. Some scholars have argued that Cimmeria rifted away from Gondwana by the opening of the Neo-Tethys ocean along the eastern margin of Gondwana during the Permian (e.g., Muttoni, Gaetani, et al., 2009; Sepehr & Cosgrove, 2004). Yet another scenario interprets Iran as an assembly of continental microplates that detached from Gondwana at different times and collided progressively with the active southern margin of Eurasia during the Mesozoic (Boulin, 1991; Golokna, 2004). Common to all

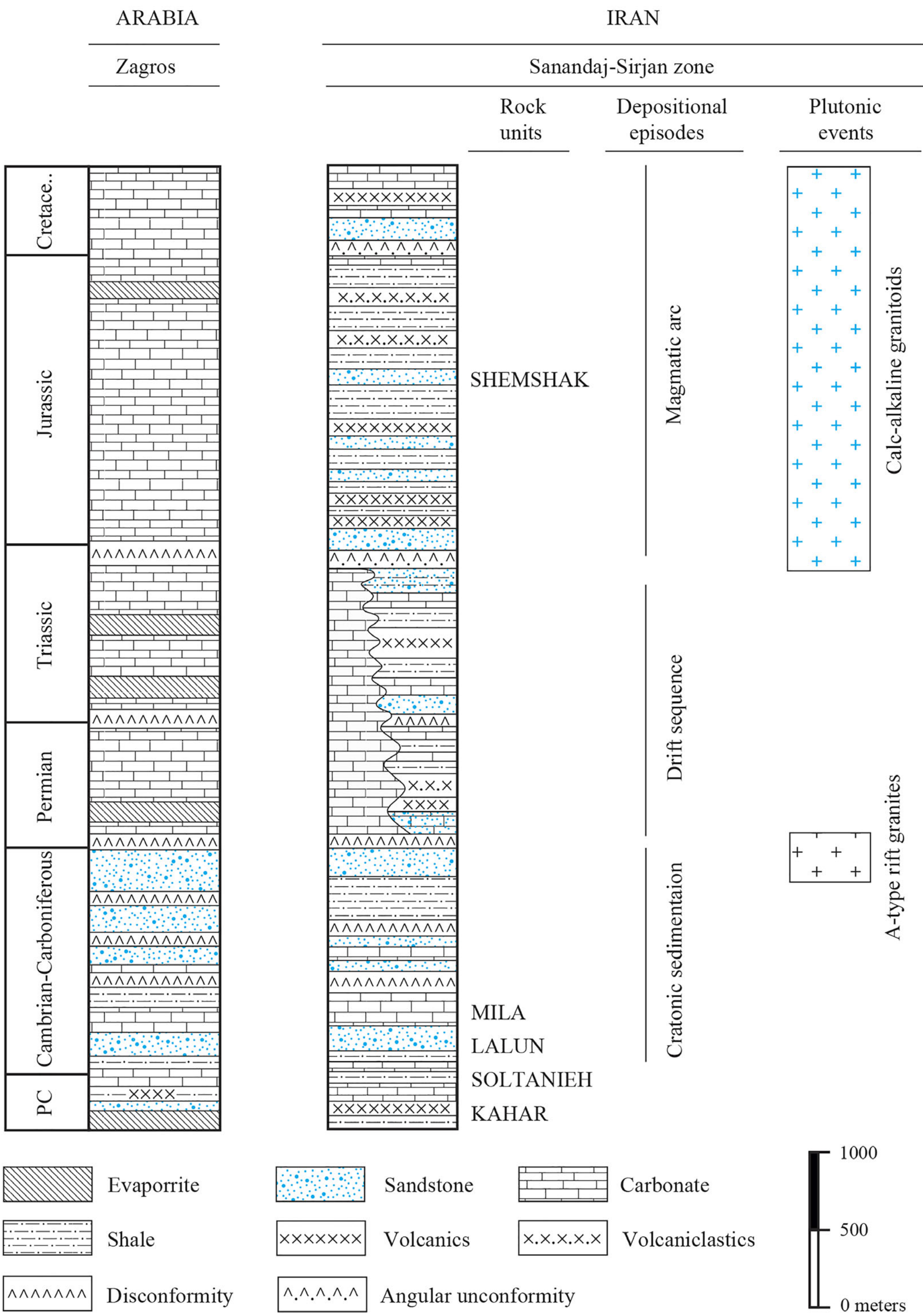

FIGURE 1 Simplified stratigraphic columns and tectonomagmatic events for late Neoproterozoic through Early Cretaceous time for the Zagros (Arabia) and Sanandaj-Sirjan zone (Iran); indicating a similar Proterozoic-Palaeozoic sequence (Modified after Hassanzadeh & Wernicke, 2016)

interpretations, however, is the fact that Iran is part of a microplate that broke away from Gondwana and drifted northwards to collide with Eurasia. Remnants of Palaeo- and Neo-Tethys, and evidence for the tectonic processes involved, are now preserved in Iran as suture zones, fold-thrust belts, accretionary prisms, ophiolitic rocks, and volcanic arcs that mark the collision zones. In these zones can be found evidence as to when, and by the opening of which ocean, Iran ultimately became detached from the Gondwanan landmass.

Although A-type granitoids are commonly insignificant volumetrically compared to other type rocks, they can be key to reconstructing

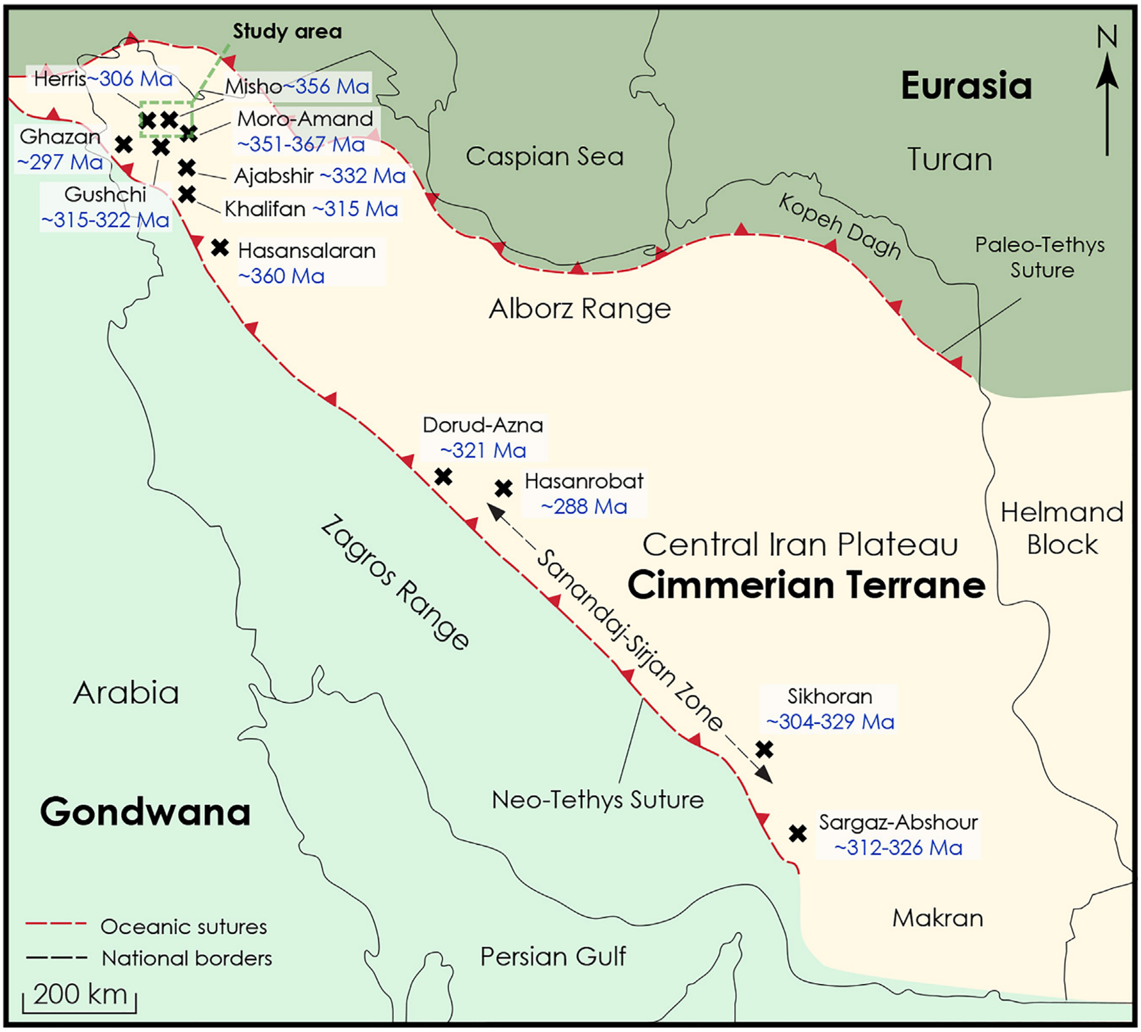

FIGURE 2 Simplified structural map of Iran, with the location of the Iranian Cimmeria Terrane between Gondwana in the south and Eurasia in the north (modified after Stampfli, Mosar, Favre, Pillevuit, & Vanney, 2001). Marked locations are the Late Palaeozoic within-plate extensional-related rocks along the Sanandaj-Sirjan Zone. Further information is presented in Table 1

and understanding a tectonic event. A-type rocks were first recognized by Loiselle and Wones (1979) as anorogenic, anhydrous, and alkaline rocks that occur in rift zones and stable continental blocks, and crystallized under low H_2O and O_2 fugacities. Subsequent studies of such rocks have expanded on the original concept (e.g., Bonin, 2007; Clemens, Holloway, & White, 1986; Collins, Beams, White, & Chappell, 1982; King, Chappell, Allen, & White, 2001; Pearce, Harris, & Tindle, 1984; Whalen, Currie, & Chappell, 1987). Eby (1992) divided A-type granitoids into two subgroups, A_1 and A_2, according to their trace element contents and geochemically inferred tectonic settings. The A_1 granitoids have chemical similarities to ocean island basalts and were inferred to be a fractionated product derived from the mantle. The A_2 granitoids are more diverse, with chemical features ranging from those of continental crust to island arc basalt. They were inferred to originate variously by melting of continental crust, underplated crust, or the mantle (with crustal interaction). It is generally considered that A-type magmas are produced in extensional tectonic settings, although the extensional regimes for the A_1- and A_2-type granitoids are significantly different (e.g., Eby, 1992). A_1-type magmas form mostly in a within-plate setting marking, for example, the initiation of intra-continental rifting. A_2-type magmas are associated with post-collisional extensional regimes, where they mark the ending of an orogeny. These distinctions make A-type rocks, their age distribution, and formation mechanisms important evidence for geological events and tectonic reconstructions. In the present work, we report zircon U–Pb ages and bulk-rock major, and trace element compositions from the Carboniferous Misho A-type granites of NW Iran. The tectonic implications of the granites along with previously studied Late Palaeozoic magmatic rocks of Iran are investigated within the context of the detachment of the Cimmerian Terrane from Gondwana by opening of Neo-Tethys.

2 | GEOLOGICAL BACKGROUND AND FIELD RELATIONSHIPS

Iran is part of the Alpine-Himalayan orogenic belt that extends from the Atlantic Ocean to the Western Pacific. The main Alpine mountain belt turns sharply south-eastwards from eastern Turkey into Iran, where it divides into two branches (Eghbal, Hamzehpour, & Farpoor, 2018). The southern branch of the system, 400–600 km in width, forms the Zagros Range, which runs along the Iraq-Iran border to Makran, then extends eastwards into southwest Pakistan, a distance of about 1,300 km. The northern branch is the Alborz Range. It is 60–130 km wide and runs for a distance of 960 km. The eastern end of the Alborz Range merges into a broader belt of mountains, the Kopeh Dagh that follows the north-eastern border of Iran and extends into northern Afghanistan, where it eventually joins the Hindu Kush. Based on the locations of basement units and ophiolite-bearing sutures in Iran, three major structural units have been distinguished (Berberian & King, 1981), the Zagros orogenic belt (Zagros ranges), Central Iran, and the Alborz orogenic belt (Alborz ranges; Figure 2). The Cimmerian Terrane, which includes the Central Iranian Plateau, is enclosed between two active marginal fold-thrust mountain belts, the Zagros to the southwest and the Alborz to the north (Figure 2). The boundary between Eurasia to the north (Hercynian realm) and ex-Gondwanan Cimmeria to the south (Alpine realm) is the Palaeo-Tethys Suture. The southern boundary of Cimmeria is the Neo-Tethys Suture.

The area of the present study, located to the southwest of Marand in the Misho Mountains of north-western Iran, is near the western end of the Central Iranian Plateau (Figure 2). The area is bounded to the north and south by two sub-parallel, dextral oblique-slip, Cenozoic fault systems, and the North and South Misho Faults, which uplifted Precambrian to Jurassic units as a major positive flower structure (Moayyed & Hosseinzade, 2011; Figure 3). The basement rocks in the Misho Mountains mostly belong to the Late Proterozoic Kahar Formation – shale, sandstone, and tuff locally intercalated with limestone (Figure 3; Asadian, Mirzaee, Mohajjel, & Hadjalilu, 1994). The Misho area consists of distinct plutonic units that have been

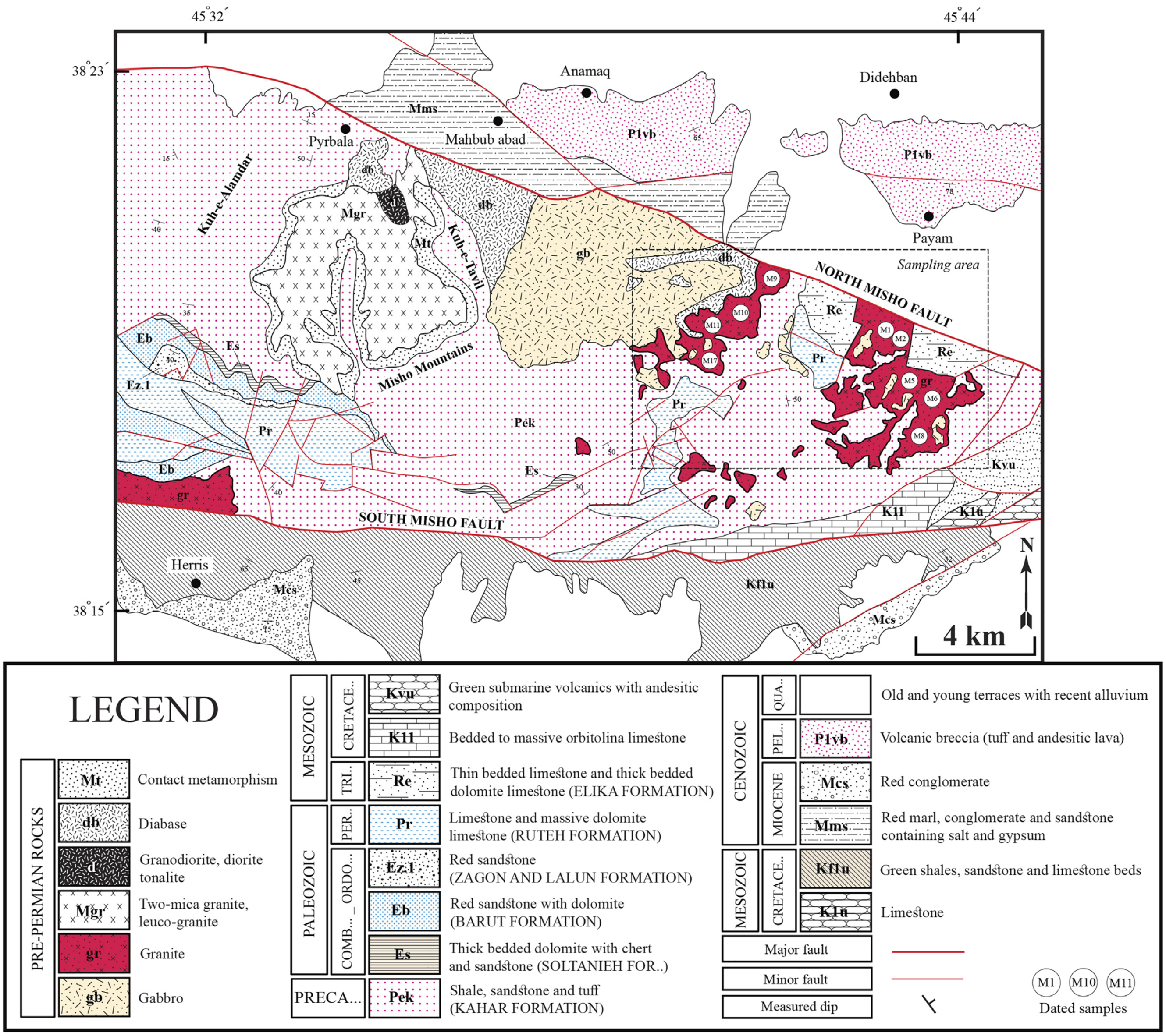

FIGURE 3 Sketch geological map of the study area

separated into four major groups. All igneous associations are unconformably overlain by the Permian cover sequence includes dark grey limestone and massive dolomitic limestone (Ruteh Formation). Hence, they are known to be pre-Permian in age on the basis of stratigraphic evidence. The first group, as small outcrops, are composed mainly of diorite, granodiorite, and tonalite. The rocks of the second group are exposed in a large area made up by two-mica granite and leucogranite. The contact between both groups is gradational, without sharp intrusive contact between them. Both groups were emplaced in the northwestern part of the area and the contact zone between those and the Kahar Formation is characterized by a wide thermal metamorphic aureole, ranging from garnet-bearing to cordierite-biotite hornfels (Asadian et al., 1994). Zircon U–Pb dating by Shahzeidi et al. (2017) indicates that the crystallization age of both groups of intrusions is ~550 Ma (Early Ediacaran). The third group, mapped as granite (Figure 3), occupies an area of about 30 km^2 and it has sharp contact with mafic and sedimentary Precambrian rocks. The granites, as the intrusion studied here, are pink to grey in colour and are massive and relatively undeformed. Granites intruded into mafic and diabase units and contain xenoliths and mafic magmatic enclaves in some places (central part). The fourth group is characterized by a mafic complex, which forms the largest body in the study area and consists of gabbro and subordinate diorite (Saccani et al., 2013; Figure 3). The complex is cross-cut by diabase dyke swarms, and dykes' of all igneous associations, suggesting that it is older than Ediacaran. Zircon U–Pb ages reported by Saccani et al. (2013), however, indicate an emplacement age of ˜356 Ma (Early Carboniferous) for the Misho mafic complex (Table 1). It is likely, therefore, that there are at least two generations of mafic rocks, distinguishing, which will require more detailed investigation.

3 | SAMPLES AND ANALYTICAL PROCEDURES

3.1 | Major and trace elements

Following a microscopic study of 20 thin sections prepared from the granitic rocks, nine representative samples with the least amount of late hydrothermal alteration were chosen. These were chipped by hand-splitter and powdered in a tungsten-carbide ring mill to a grain size of <200 mesh. Aliquots of each powder were sent to the ALS (Australian Laboratory Services) Brisbane laboratory, Australia, for whole-rock analysis by the geochemistry method ME-MS81d (ME-MS81 plus whole rock). Major oxide concentrations were done by Inductively Coupled Plasma-Atomic Emission (ICP-AES) and trace elements were carried out by Inductively Coupled Plasma Mass Spectrometry (ICP-MS). For this purpose, 0.2 g of sample powder is added to 1.5 g lithium metaborate ($LiBO_2$), mixed well, and fused in a furnace at 1,000°C. The resulting melt is then cooled and dissolved in 100 ml of 5% HNO_3 acid solution. This solution is then analysed either by ICP-MS and ICP-AES. The accuracy of major elements is 0.01%, for most trace elements, it is better than 10 ppm and for the rare earth elements (REE), it is 0.1 ppm or better. The results are listed in the Supporting Information.

3.2 | SHRIMP zircon U–Pb dating

Three samples from different regions, each weighing 0.5–1 kg, were selected for zircon separation and U–Pb dating at the Research School of Earth Sciences (RSES), Australian National University (ANU). Zircon concentrates were prepared using standard high-cleanliness mineral separation techniques, mechanical chipping, ultrasonic washing, tungsten-carbide milling, magnetic separation by Carpco magnetic separator, density separation in tetrabromoethane and methylene iodide, and division into heavy-mineral fractions using a Frantz isodynamic separator. Clean zircon crystals were then hand-picked from the remaining minerals under a binocular microscope. They, together with zircon standards, were mounted in epoxy resin discs and polished to expose cross sections of the crystals and produce a flat surface for analysis, first by polishing on 1,200 grade SiC wet-and-dry abrasive paper, and then using a series of diamond emulsions from 3 μm down to 1 μm on a Struers Labopol-5 rotary polisher. The mounts were then photographed at high magnification under transmitted and reflected light, before being lightly coated with Au in preparation for cathodoluminescence (CL) imaging. Those images, acquired using a JEOLJSM-6610A at the RSES, revealed the internal textures and growth zoning of each zircon grain, and helped to locate areas free from inclusions and fractures that would be suitable for spot isotopic analysis.

The U–Pb isotopic analyses (Supplementary file) were performed using the SHRIMP-RG (Sensitive High-Resolution Ion Microprobe), following the analytical procedure described by Williams (1998). U concentrations were determined using reference zircon SL13 (238 ppm U, ˜572 Ma) and Pb/U measured relative to reference zircon TEMORA 2 (417 Ma; Black et al., 2004). The radiogenic isotope ratios and calculated ages were corrected for common Pb using the measured ^{207}Pb, assuming concordance and a model common Pb composition consistent with the age of the grain (Cumming & Richards, 1975) using Prawn and Lead software written by Ireland (1998). All individual dates and weighted mean ages were calculated from the radiogenic ^{206}Pb/^{238}U. Data were plotted using Isoplot 3 (Ludwig, 2003), showing the analyses before correction for common Pb. For all analyses, the uncertainty in the determination of Pb/U and Pb/Th was set to a minimum of 0.5% to prevent the high precision analyses of high-U spots skewing the calculation of the weighted mean ages. The uncertainties listed in the Supporting Information and plotted in Figure 6 are 1δ precision estimates. The uncertainties in the calculated weighted mean age of each sample are 95% confidence limits (tδ) and include the uncertainty in the mean concurrent measurement of ^{206}Pb/^{238}U in TEMORA 2 (~0.35%).

4 | ANALYTICAL RESULTS

4.1 | Major and trace element compositions

The chemical compositions of the analysed samples from the Misho granite are listed in the Supporting Information. All samples are high silica (71.4–77.7 wt% SiO_2), high-K alkali-calcic (8.57–9.53 wt% K_2O

TABLE 1 Late Palaeozoic within-plate extensional-related rock association's geochronology in the Sanandaj-Sirjan Zone

Pluton	Suite	Type	Method	Age (Ma)	Error	Period	Tectonic setting	References
Hasanrobat	Granite	A (A_1)	U–Pb	288.3	3.6	Early Permian	Within-plate Extensional	Alirezaei & Hassanzadeh, 2012
	Granite	A (A_1, A_2)	U–Pb	294.2	2.5	Early Permian		Honarmand, Li, Nabatian, & Neubauer, 2017
Ghazan	Gabbro	-	U–Pb	297	6	Early Permian	Within-plate Extensional	Asadpour, Pourmoafi, & Heuss, 2013
Herris	Granite	A	U–Pb	306	34	Late Carboniferous	Within-plate Extensional	Advay & Ghalamghash, 2011
Ghushchi	Gabbronorite	A(A_1, A_2)	U–Pb	319.9	2.5	Late Carboniferous	Within-plate Extensional	Shafaii Moghadam et al., 2015a
	Gabbronorite	A (A_1, A_2)	U–Pb	316.8	2.3	Late Carboniferous		
	Granite	A (A_1, A_2)	U–Pb	318.4	2.3	Late Carboniferous		
	Granite	A (A_1, A_2)	U–Pb	317.3	1.9	Late Carboniferous		
	Granite	A (A_1, A_2)	U–Pb	322	2.9	Late Carboniferous		
Khalifan	Granite	A	U–Pb	315	2	Late Carboniferous	-	Bea, Mazhari, Montero, Amini, & Ghalamghash, 2011
Dorud-Azna	Metagabbro	-	U–Pb	314.6	3.7	Late Carboniferous	Within-plate Extensional	Shakerardakani et al., 2015
Sargaz-Abshour	Orthogneiss	-	U–Pb	312.2	4.1	Late Carboniferous	Extensional Regime	Shafaii Moghadam et al., 2017
Sikhoran	Gneiss	-	K-Ar	304.9	7	Late Carboniferous	Within-plate Extensional	Ghasemi et al., 2002
Misho	Leucogabbro	-	U–Pb	356.7	3.4	Early Carboniferous	Within-plate Extensional	Saccani, Azimzadeh, Dilek, & Jahangiri, 2013
Amand	Granite	A (A_2)	U–Pb	350.9	1.3	Early Carboniferous	Within-plate Extensional	Mohammadi, Moazzen, Lechmann, & Laurent, 2019
Dorud-Azna	Mafic Dyke	-	Ar-Ar	321.3	0.55	Early Carboniferous	Within-plate Extensional	Shakerardakani et al., 2015
Sargaz-Abshour	Orthogneiss	-	U–Pb	318.7	4	Early Carboniferous	Extensional Regime	Shafaii Moghadam et al., 2017
	Orthogneiss	-	U–Pb	326.3	3.3	Early Carboniferous		
Sikhoran	Granite	Anatectic	K-Ar	329.6	7.6	Early Carboniferous	Within-plate Extensional	Ghasemi et al., 2002
	Amphibolite	-	K-Ar	324.6	16.6	Early Carboniferous		
Ajabshir	Rhyolite	A (A_1)	U–Pb	332.5	2.2	Early Carboniferous	Within-plate Extensional	Nabatian, Li, Honarmand, & Esmaeili, 2021
Hasansalaran	Granite	A (A_1)	U–Pb	360.3	4.3	Late Devonian	Within-plate Extensional	Azizi, Kazemi, & Asahara, 2017
	Granite	A (A_1)	U–Pb	360.7	5.6	Late Devonian		
Moro	Granite	A (A_2)	U–Pb	366.8	6.8	Late Devonian	Within-plate Extensional	Mohammadi et al., 2019

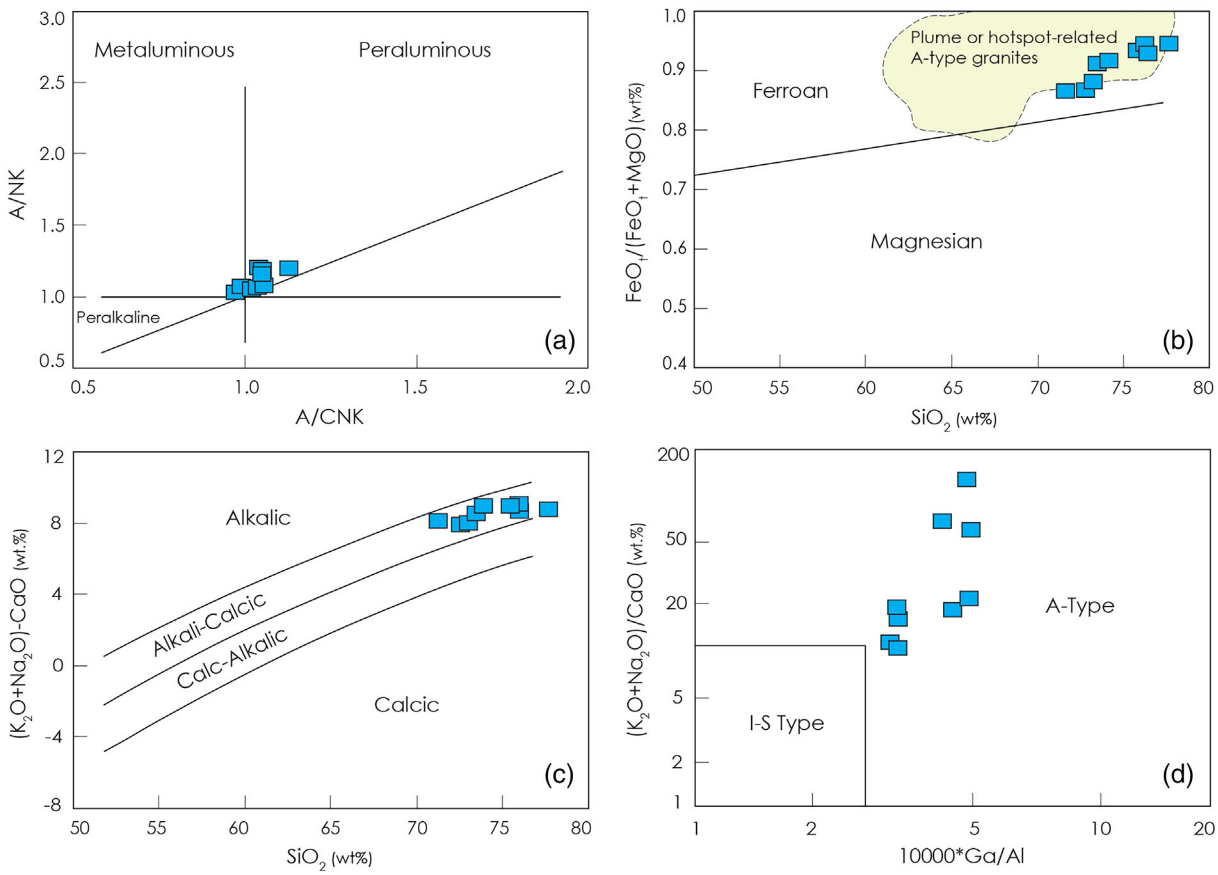

FIGURE 4 (a) Peraluminous, metaluminous and peralkaline discrimination by molar $Al_2O_3/CaO + Na_2O + K_2O$ (A/CNK) versus $Al_2O_3/Na_2O + K_2O$ (A/NK) ratios (Maniar & Piccoli, 1989); (b) $FeO_t/(FeO_t + MgO)$ versus SiO_2 and (c) $(K_2O + Na_2O)$-CaO versus SiO_2 diagrams (Frost et al., 2001); (d) $(K_2O + Na_2O)/CaO$ and Nb versus 10,000*Ga/Al discrimination diagram (Whalen et al., 1987). Hotspot or plume-related A-type granites field is from Wang et al. (2010)

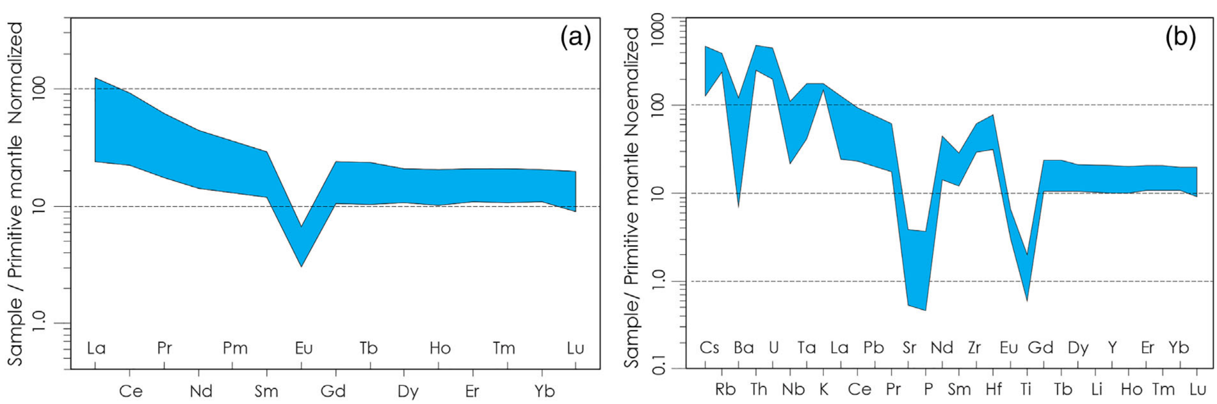

FIGURE 5 Plots of trace element distributions in various types of granitoids from the Misho complex. (a, c, e) Primitive mantle-normalized rare earth element (REE) compositions; (b, d, f) Primitive mantle-normalized multi-element patterns. REE and multi-elements normalizing values are from McDonough and Sun (1995) and Sun and McDonough (1989) respectively. Profiles of the Misho gabbros are from Saccani et al. (2013) and profiles of the Misho I and S-type granites and leucogranites are from Shahzeidi et al. (2017)

$+ Na_2O$), weakly metaluminous to peraluminous (0.74–1.11 A/CNK and 1.02–1.2 A/NK), ferroan granites with characteristically high $(K_2O + Na_2O)/CaO$ and Ga/Al (Figure 4) that distinguishes them as A-type granites (Whalen et al., 1987). The rocks are enriched in total REE (116–399 ppm), and particularly the light REE (Figure 5a), with high La_N/Yb_N (2.19–8.06), a pronounced negative Eu-anomaly ($Eu/Eu^* = 0.16$–0.36) and relatively flat and undifferentiated heavy REE ($Gd_N/Yb_N = 0.96$–1.53). The high La_N/Sm_N (2.55–4.11) is consistent

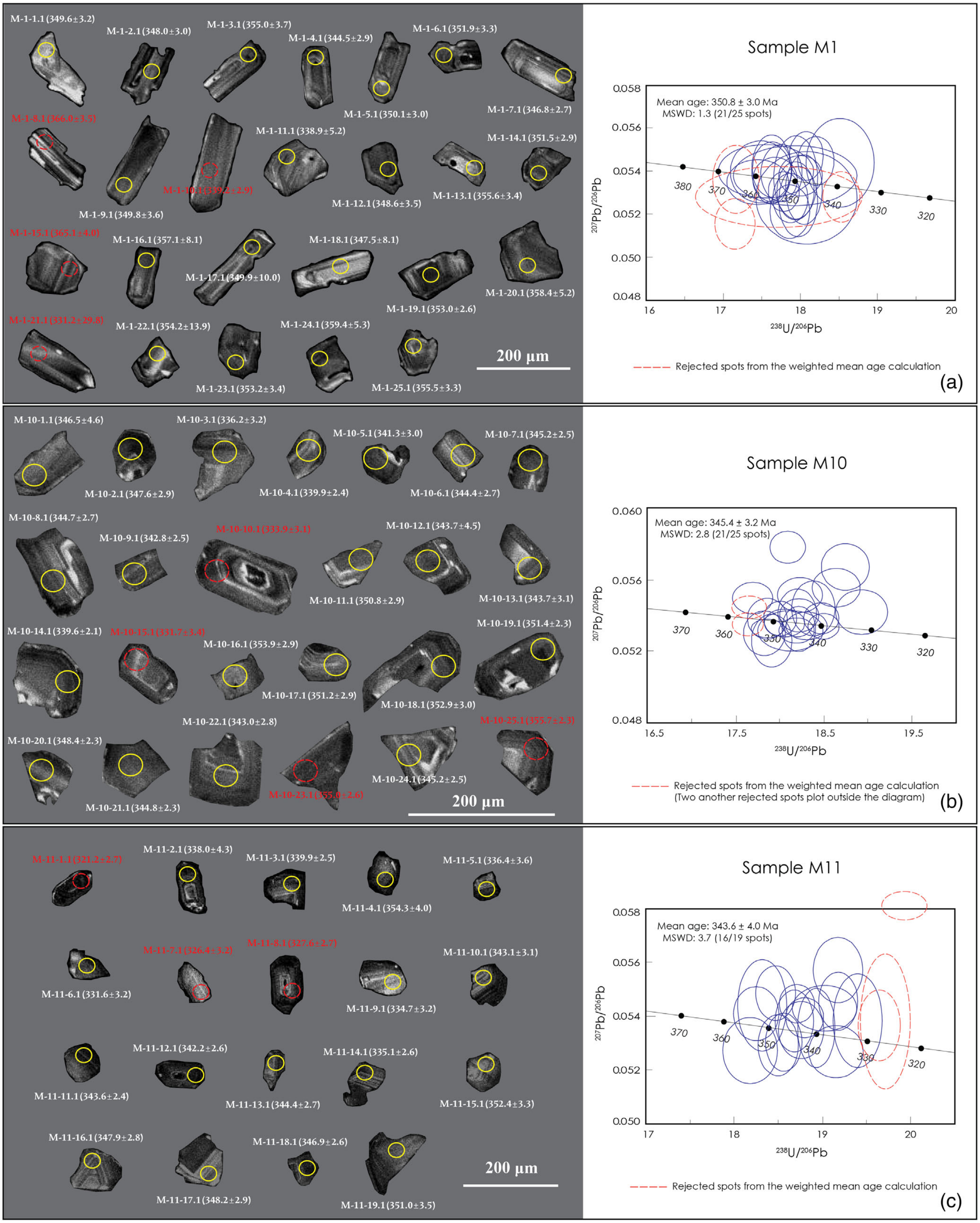

FIGURE 6 Representative zircon cathodoluminescence (CL) images of analysed spots from samples M-1 (a), M10 (b), and M11 (c). Brighter fluorescing domains are relatively depleted in U and Th while areas with darker fluorescing are richer in these trace elements. Most of the spots in each of the three samples give concordant or nearly concordant U–Pb ages. Nevertheless, some spot analyses are discordant in their U–Pb system (red circles). Discordant spots overlap both the oscillatory zoned and CL bright zircon, likely representing a mix between the two areas in the zircon with different ages. However, some of them do not appear to be associated with these areas and may be related to spots analysed in the region of large inclusions. The inclusions apparently act as local Pb sinks enhancing diffusion and removing Pb from the zircon so lowering the apparent U–Pb age (Bea, Montero, & Palma, 2018)

with fractionation of the LREE. The granites in the multi-element variation diagram exhibit strong negative anomalies in Ba, Sr, P, and Ti; a moderate negative anomaly in Nb and Ta; and significant enrichment in large ion lithophile elements (Rb, K, Th, and U) and high field strength elements (Ta, Zr, and Hf; Figure 5b).

4.2 | Zircon U–Pb geochronology

The three samples selected for SHRIMP zircon U–Pb dating were M1, M10, and M11. The sample locations are shown in Figure 3, and the zircon U–Th–Pb isotopic compositions are listed in the Supporting Information for samples M1, M10, and M11, respectively. The zircon grains from sample M1 were mostly euhedral to subhedral, colourless, and transparent, 50–100 μm diameter crystals with few cracks and inclusions. Simple oscillatory or banded igneous zoning was common, and no inherited cores were evident in the CL images (Figure 6a). One spot on each of 25 grains was analysed for U–Th–Pb. The grains had moderate contents of U (177–642 ppm) and Th (60–371 ppm) with Th/U ratios of 0.34–0.81, consistent with an igneous origin. Most analyses were concordant within analytical uncertainty but with minor excess scatter in radiogenic $^{206}Pb/^{238}U$ (MSWD = 3.1). Omission of two high and two low analyses resulted in a single population (Figure 6a) with a weighted mean $^{206}Pb/^{238}U$ age of 350.8 ± 3.0 Ma (MSWD = 1.3).

The zircon grains from sample M10 were mostly fragments of transparent, colourless to brownish, 50–100 μm diameter crystals, and some with cracks and inclusions. CL images of most grains showed oscillatory zoning and no evidence for the presence of older cores (Figure 6b). Some grains had irregular strongly luminescent patches, possibly representing secondary re-crystallization in the presence of fluids. One spot on each of 25 grains was analysed for U–Th–Pb. The U and Th contents were moderate to high (601–1,689 and 319–966 ppm, respectively), consistent with the rock's high SiO_2 content. Th/U (0.45–0.71) was in the normal igneous range. With few exceptions the raw analyses were nearly concordant within analytical uncertainty (Figure 6b), but there was a significant range in radiogenic $^{206}Pb/^{238}U$ (MSWD = 5.0). Only by rejecting eight analyses could the scatter be eliminated. It was reduced significantly, however, by omitting just the two highest and two lowest $^{206}Pb/^{238}U$ ages, giving a weighted mean $^{206}Pb/^{238}U$ age of 345.4 ± 3.2 Ma (MSWD = 2.8).

The zircon grains from sample M11 were subhedral to anhedral, transparent, colourless, 50–100 μm diameter crystals, many with cracks, and mineral inclusions. Most had oscillatory zoning, and none showed evidence for the presence of an older core (Figure 6c). One spot on each of 19 grains was analysed for U–Th–Pb. The U and Th contents (364–2092 and 133–1706 ppm, respectively) were even higher than in the M10 zircon, but Th/U was still within a normal igneous range (0.36–0.82). Even before common Pb correction, most analyses were concordant within analytical uncertainty (Figure 6c), but there was a significant range in radiogenic $^{206}Pb/^{238}U$ (MSWD = 9.4). The outliers were mostly low in the group, consistent with radiogenic Pb loss. Omitting the four lowest values reduced the scatter significantly (MSWD = 3.7), giving a weighted mean $^{206}Pb/^{238}U$ age of 343.6 ± 4.0 Ma.

5 | DISCUSSION

5.1 | U–Pb zircon geochronology perspective on the crystallization of the Misho pluton

Plutons are formed by protracted crystallization of magma bodies several kilometres deep within the crust. As a single pluton can crystallize over a protracted period of time (Buret et al., 2016; Samperton et al., 2015; Schoene et al., 2012; Tapster et al., 2016), a single hand sample may miss the full crystallization history of an entire pluton. The Misho pluton indicates ages ranging from ~344 to ~351 Ma (Figure 3). Zircon grains from samples M10 and M11 yield ages of 345 ± 3 and 344 ± 4 Ma, respectively. These representative samples show similar age distribution and mean ages, which suggest a simultaneous crystallization event, although morphology of zircons and also CL imaging (Figure 6b,c) may indicate faster crystallization process and cooling rates of sample M11. Besides, the sample M1 yields an age of 351 ± 3 Ma. The time interval of ~6 Ma is within uncertainty of analysis, and therefore, cannot resolve relative timing; suggesting that the crystallization in the study granitic rocks was not coeval. The ages obtained from the Herris magmatic facies in the western domain (306 Ma; Advay & Ghalamghash, 2011; Figure 3) along with dated samples reveal that the whole pluton sequentially crystallized in different stages at ca. 306–350 Ma. The apparent age gap between these magmatic pulses potentially constrains the recharge duration of the A-type pluton.

5.2 | Genetic type

The Misho granites have geochemical characteristics typical of A-type granites, most notably high abundances of incompatible elements (LILE or large-ion lithophile elements and HFSE or high field strength elements), and high $K_2O + Na_2O$, $FeO_t/(FeO_t + MgO)$, and Ga/Al, combined with low contents of CaO, P_2O_5, and pronounced negative anomalies in elements such as Ba, Sr, and Eu (e.g., Bonin, 2007; Eby, 1992; Frost et al., 2001; Whalen et al., 1987). In terms of major elements (Na, K, Fe, Ca, and Mg) they cluster tightly in the A_1 field (Figure 7a), but considering Rb, Y, and Nb, five of the nine samples analysed plot well within the A_2 field (Figure 7b). This bimodality is consistent with Ce/Nb and Y/Nb contents (Figure 7c); indicating geochemical signatures similar to both ocean island basalts and island arc basalts. However, trace element variations in A_1 and A_2-type granites suggest the same source rock (Figure 7d). It has been proposed that A_1-type granites originate from mantle-derived melts emplaced in a rift-related anorogenic setting, whereas A_2-type granites result from melting of continental or underplated crust in a post-orogenic extensional setting (Eby, 1992). More recent studies, however, have found no such correspondence. For example, some plume or hotspot-related

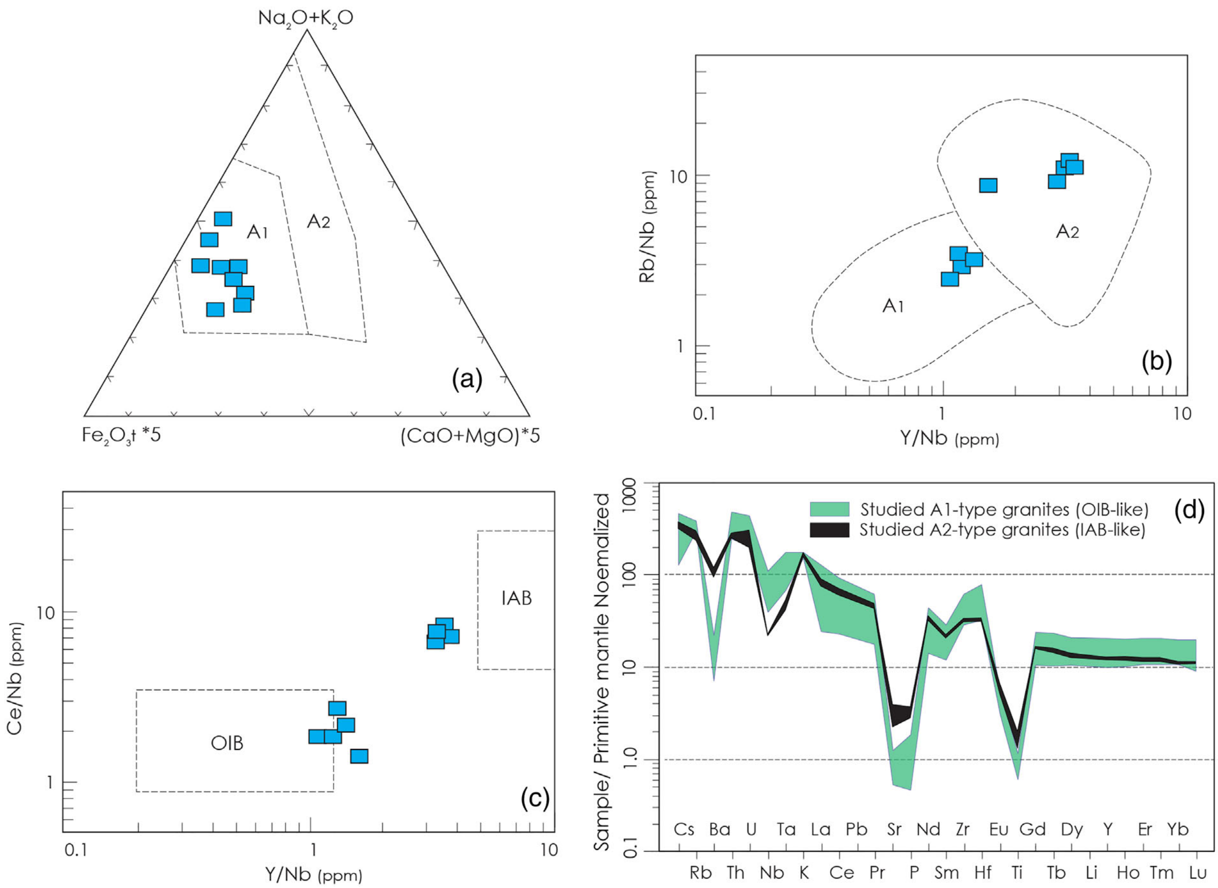

FIGURE 7 (a) Triangular diagrams of $Na_2O + K_2O$-$Fe_2O_3(t)\times5$-$(CaO + MgO)\times5$ (Grebennikov, 2014); (b) Y/Nb versus Rb/Nb diagram (Eby, 1992); (c) Y/Nb versus Ce/Nb diagram (Eby, 1990); (d and e) Variation of trace elements in A_1 and A_2-type granites. Normalized values are the same as in Figure 5

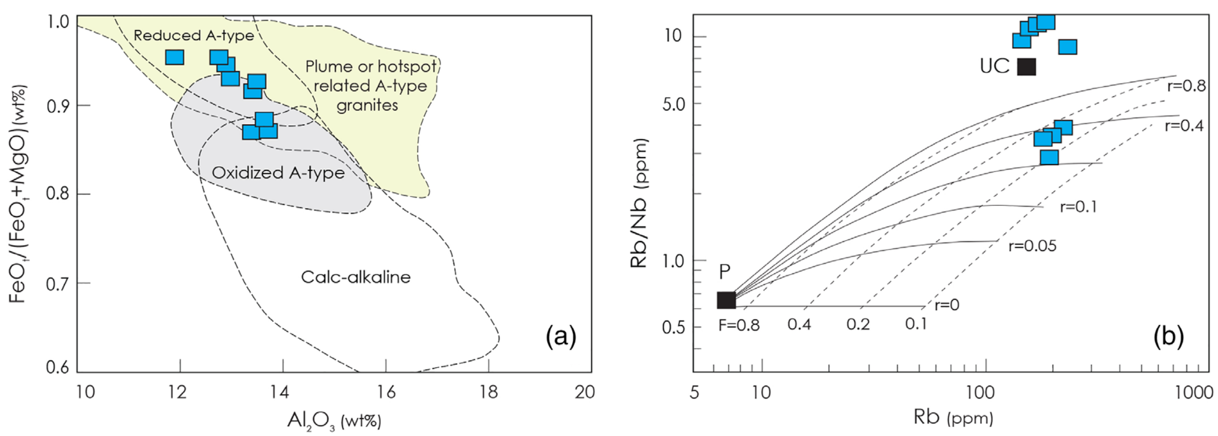

FIGURE 8 (a) Diagram of $FeO_t/(FeO_t + MgO)$ versus Al_2O_3 (Dall'Agnol & de Oliveira, 2007). Hotspot or plume-related A-type granites field is from Wang et al. (2010); (b) Rb versus Rb/Nb diagram (Pearce et al., 1990). The modelling was conducted using the assimilation and fractional crystallization equations of DePaolo (1981) P: parental basaltic magma compositions (Pearce et al., 1990), UC: composition of average upper crust (Taylor & McLennan, 1985), r: ratio of assimilation to fractional crystallization, F: fractional crystallization ratio

A-type granitoids plot in both the A_1- and A_2-type fields (e.g., Frost, Frost, Chamberlain, & Edwards, 1999; Haapala, Frindt, & Kandara, 2007; Shellnutt & Zhou, 2007; Trumbull, Harris, Frindt, & Wigand, 2004; Wang et al., 2010), and some typical anorogenic A-type granites plot in the A_2-type field (e.g., Dall'Agnol et al., 2005). The chemical composition of the Misho granites, ranging as it does between both fields, is therefore, not a clear indicator of tectonic setting or likely magma source. A more useful indicator is the similarity between the A-type granite trace element patterns and those of the older Misho S-type granites, consistent with the two being genetically linked through a source that contained continental crust.

The oxygen fugacity (fO_2) of igneous rocks is closely related to the composition and oxidation state of their source rocks. Experimental data show that A-type magmas contain dissolved OH–F-bearing fluids (e.g., Bonin, 2007; Clemens et al., 1986; Dall'Agnol, Scaillet, & Pichavant, 1999; Klimm, Holtz, Johannes, & King, 2003), so fO_2 plays an important role in understanding their nature and petrogenesis (e.g., Anderson & Morrison, 2005; Christiansen, Haapala, & Hart, 2007; Dall'Agnol & de Oliveira, 2007). $FeO_t/(FeO_t + MgO)$ in the Misho A-type granites ranges from 0.87 to 0.95, spanning the range from reduced to weakly oxidized (Figure 8a). In this and some other geochemical respects, they are similar to typical mantle plume-related A-type granitoids generated in anorogenic or rift settings (Figures 4b and 8a). Considering that the fO_2 of a magma or its source is particularly resistant to change (Carmichael, 1991), a source with low fO_2 cannot produce magmas with high fO_2. The range of fO_2 in the Misho A-type granites is possibly the result of reduced granitic magmas interacting with felsic continental crust (Figure 8b), producing the oxidized or peraluminous members of the granite suite (Frost et al., 1999).

5.3 | Geodynamic implications

Palaeogeographic reconstructions indicate that the formation of both Palaeo- and Neo-Tethys played a key role in the evolution of the Iranian continent during the break-up of the northern margin of Gondwana (Figure 2).

5.3.1 | Palaeo-Tethys ocean

The most commonly-held view is that the Palaeo-Tethys began to open in the Ordovician to Silurian (Li et al., 2018; Stampfli et al., 2001; Topuz et al., 2020; von Raumer et al., 2013; Ziegler, Cloetingh, Guiraud, & Stampfli, 2001) as a intra-continental rift between a fringe of microplates (the Hun or Hunic superterrane) and the Gondwana-derived continental fragments of the Cimmerian Terrane (Stampfli & Borel, 2002; von Raumer & Stampfli, 2008). The Cimmerian Terrane moved northwards towards Eurasia, driven by northward subduction of the Palaeo-Tethys oceanic crust beneath the southern Eurasian (Turan) margin, finally colliding with the southern boundary of Eurasia in the Late Triassic (e.g., Bagheri & Stampfli, 2008; Liu, Jian, Kroner, & Xu, 2006; Stampfli et al., 2001; Stampfli & Borel, 2002). The onset of Palaeo-Tethys opening and its closure are well recorded in northern Iran. Ordovician–Silurian rift-related continental flood basalts of the Soltan-Meidan area in the Alborz record the opening of the Palaeo-Tethys rift (Bagheri & Stampfli, 2008) and the Middle to Late Palaeozoic Dareh-Anjir ophiolites and ultramafic to mafic rocks in the Mashhad and Fariman areas (Shafaii Moghadam et al., 2015b; Topuz, Hegner, Ackerman, Pfänder, & Karimi, 2018) formed in a fore-arc area (Zanchetta et al., 2013) record its closure as the Cimmerian blocks collided with Eurasia.

The Early Jurassic coal-bearing continental clastic deposits to the north and south of the collisional zone indicate that by the Late Triassic to Early Jurassic Palaeo-Tethys ceased to exist and Iran-Turan was united (Berberian & King, 1981). Other workers suggest that Palaeo-Tethys opened initially much later. Saccani et al. (2013) have argued that the initial opening of the Palaeo-Tethys Ocean took place in the Early Carboniferous, coincident with the formation of the mafic units at Misho by an upwelling mantle plume. Similarly, Mohammadi et al. (2019) suggested that the Palaeo-Tethys opened during the Late Devonian–Carboniferous associated with mantle upwelling and a rising asthenosphere plume that generated the Amand and Moro A-type plutons. This timing is earlier than indicated from evidence in other areas including north Iran.

5.3.2 | Neo-Tethys ocean

The northward subduction of Palaeo-Tethys triggered the opening of Neo-Tethys, a younger ocean, along the boundary between the Cimmerian blocks and Gondwana. This resulted in the separation of the Iranian Terrane, part of the large composite Cimmerian Terrane, from the Arabian margin of Gondwana. The timing of the opening of Neo-Tethys and the detachment of the Cimmerian Terrane from Gondwana is debated. According to some authors, Iran drifted northward as part of the Cimmerian blocks following the opening of Neo-Tethys in the Permian to Early Triassic (e.g., Muttoni, Gaetani, et al., 2009; Sengor, 1990; Sepehr & Cosgrove, 2004). Others interpret the initial opening of the Neo-Tethys ocean to have occurred earlier, in the Early Permian (e.g., Angiolini, Balini, Garzanti, Nicora, & Tintori, 2003; Berra & Angiolini, 2014; Honarmand et al., 2017; Muttoni et al., 2009; Riel, Jaillard, Martelat, Guillot, & Braun, 2018; Zanchi et al., 2009). Yet others consider an ocean that opened in the Late Carboniferous to late Early Permian to be the Neo-Tethys (e.g., Arefifard, 2017; Stampfli, 2000; Stampfli & Borel, 2002). Late Palaeozoic rock associations of Iran are key to reconstructing the evolution of the Neo-Tethys Ocean. They define a trend parallel to the Neo-Tethys suture, and all have been interpreted to be emplaced in a within-plate extensional tectonic setting (Figure 2; Table 1 and references therein). The ages obtained from these rocks (Table 1 and Figure 6) reveal that the rifting of the Iranian Cimmerian terranes from northern Gondwana and the opening of the Neo-Tethys Ocean was probably initiated in the Late Devonian to Early Carboniferous, rather than the Late Carboniferous to Early Permian, as most authors suggest (Figure 9).

Stratigraphic correlation of the Silurian to Devonian rock units from Iran and Arabia suggests the Central Iran and Arabian Plate together formed a stable shield, forming the northern margin of Gondwana (Hashmie et al., 2016). The lack of Silurian to Carboniferous strata along the Central Zagros and the existence of terrigenous sediments of the Sare-Chahan (Silurian) and Zakeen (Upper Devonian) formations in the Zagros Crush Zone indicate that the Zagros area was

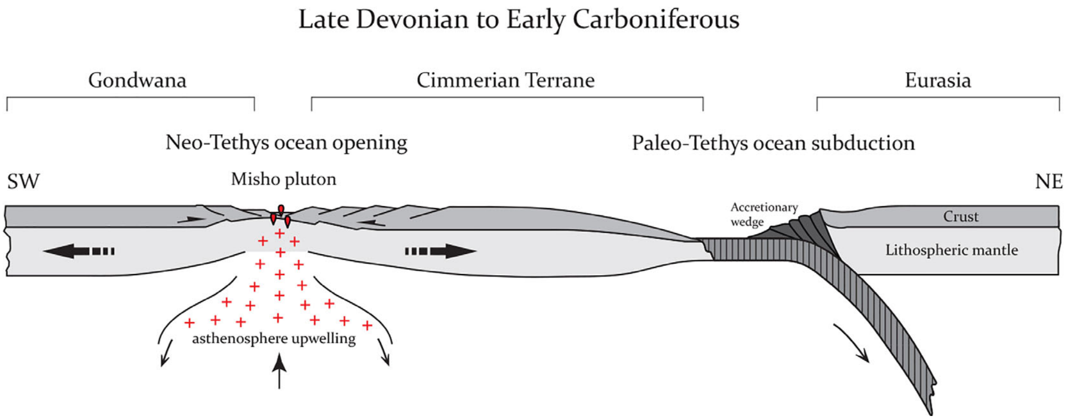

FIGURE 9 Schematic cross-section, illustrating the evolution model for the Neo-Tethys opening

elevated and eroding, possibly because the Neo-Tethys plume was emplaced beneath the lithosphere of Gondwana and led to uplift between Central Iran and the Arabian Plate during that time interval (Ajirlu, Moazzen, & Hajialioghli, 2016). The rising magmatic plumes and their underplating can cause swelling and bulging of the lithosphere and tensile stresses in the domed area (Fossen, 2010). This stage refers to rift initiation by thermal buoyancy forces due to asthenospheric upwellings (Kearey, Klepeis, & Vine, 2009) and the result is a rift dominated by magmatism and not necessarily much extension (Fossen, 2010). At least since the Early Carboniferous to Early Permian eruption of plume magmas (include Misho pluton and suites provided in Table 1) along the Neo-Tethys rift zone indicate that the Iran and Arabia stable shield was rifting into two parts: Central Iran and the Arabian Plate (Figure 9). During the early stages of rifting, the basin was almost dry or contained freshwater lakes (Hanblin & Christiansen, 1997). Eventually, the floor of the Neo-Tethys subsided and formed a shallow-water sedimentary basin during the Late Carboniferous–Early Permian. This basin is shown by the deposition of evaporates and terrigenous sediments of the Faraghan (Late Carboniferous to Lower Permian) and Dalan (Upper Permian) formations (Ajirlu et al., 2016). Thereafter, the extension of the basin continued and continental rifting led to the spreading and maturation of the Neo-Tethys oceanic basin during the Late Permian–Late Triassic. The subsidence of the basin floor led to the formation of a passive margin on each side of the oceanic rift, located in oceanic crust.

6 | CONCLUSIONS

The main conclusions from the present study are as follows:

1. The Misho A-type granites are weakly metaluminous to weakly peraluminous. They belong primarily to the reduced A_1 subtype, although they have some chemical features of the A_2 subtype, consistent with their being within-plate anorogenic granites associated with crustal extension and/or rifting.
2. The zircon U–Pb ages of the granitic rocks, 345–350 Ma, support the hypothesis that rifting forming the Neo-Tethys Ocean and the consequent detachment of the Iranian Cimmerian Terrane from Gondwana was initiated at least in the Early Carboniferous, earlier than previously proposed.
3. The ages obtained from the granitic rocks from the whole A-type pluton (Misho and Herris) reveal that the crystallization process took place sequentially in different stages.

ACKNOWLEDGEMENTS

Most of the laboratory work was carried out at Research School of Earth Sciences, Australian National University. We would like to thank Prof. Trevor Ireland for providing access to the RSES ion microprobe facilities, Prof. Vickie C. Bennett for her support with elemental analyses, and Mr. Shane Paxton for his assistance with zircon separation. This paper greatly benefited from the insightful and constructive comments by Prof. Carol Frost, Prof, Aral Okay, Dr. Gültekin Topuz, Dr. Chris Fergusson, and two anonymous reviewers. We are also very grateful to Dr. Erdin Bozkurt for editorial handling.

CONFLICT OF INTEREST

All authors declare there is no conflict of interest.

DATA AVAILABILITY STATEMENT

The data that supports the findings of this study are available in the supplementary material of this article.

ORCID

Susan Jamei https://orcid.org/0000-0003-0199-1523

REFERENCES

Advay, M., & Ghalamghash, J. (2011). Petrogenesis and U–Pb dating zircon of granites of Herris (NW of Shabestar), eastern Azerbaigan Province. *Iranian Journal Crystallography Mineralogy*, *4*, 633–648.

Ajirlu, S. M., Moazzen, M., & Hajialioghli, R. (2016). Tectonic evolution of the Zagros Orogen in the realm of the Neotethys between the Central Iran and Arabian plates: An ophiolite perspective. *Central European Geology*, *59*, 1–27. https://doi.org/10.1556/24.59.2016.001.

Alirezaei, S., & Hassanzadeh, J. (2012). Geochemistry and zircon geochronology of the Permian A-type Hasanrobat granite, Sanandaj–Sirjan belt: A new record of the Gondwana break-up in Iran. *Lithos*, *151*, 122–134. https://doi.org/10.1016/j.lithos.2011.11.015.

Anderson, J. L., & Morrison, J. (2005). Ilmenite, magnetite, and peraluminous Mesoproterozoic anorogenic granites of Laurentia and Baltica. *Lithos*, *80*, 45–60. https://doi.org/10.1016/j.lithos.2004.05.008.

Angiolini, L., Balini, M., Garzanti, E., Nicora, A., & Tintori, A. (2003). Gondwanan deglaciation and opening of Neotethys: The Al Khlata and Saiwan formations of interior Oman. *Palaeogeography*, *Palaeoclimatology*, *Palaeoecology*, *196*, 99–123. https://doi.org/10.1016/S0031-0182(03)00315-8.

Arefifard, S. (2017). Foraminiferal-based paleobiogeographic reconstructions in the Carboniferous of Iran and its implications for the Neo-Tethys opening time: A synthesis. *Geologica Acta*, *15*, 135–151. https://doi.org/10.1344/GeologicaActa2017.15.2.5.

Asadian, Q., Mirzaee, A. R., Mohajjel, M., & Hadjalilu, B. (1994). *Geological map of Marand, No. 5166, 1/100 000 scale*. Tehran, Iran: Geological Survey of Iran.

Asadpour, M., Pourmoafi, S. M., & Heuss, S. (2013). Geochemistry, petrology and U-Pb geochronology of Ghazan mafic-ultramafic intrusion, NW Iran. *Petrology*, *4*(14), 1–16 (in Persian with English abstract).

Azizi, H., Kazemi, T., & Asahara, Y. (2017). A-type granitoid in Hasansalaran complex, northwestern Iran: Evidence for extensional tectonic regime in northern Gondwana in the Late Paleozoic. *Journal of Geodynamics*, *108*, 56–72. https://doi.org/10.1016/j.jog.2017.05.003.

Bagheri, S., & Stampfli, G. M. (2008). The Anarak, Jandaq and Posht-e-Badam metamorphic complexes in central Iran: New geological data, relationships and tectonic implications. *Tectonophysics*, *451*, 123–155. https://doi.org/10.1016/j.tecto.2007.11.047.

Bea, F., Mazhari, A., Montero, P., Amini, S., & Ghalamghash, J. (2011). Zircon dating, Sr and Nd isotopes, and element geochemistry of the Khalifan pluton, NW Iran: Evidence for Variscan magmatism in a supposedly Cimmerian superterrane. *Journal of Asian Earth Sciences*, *40*, 172–179. https://doi.org/10.1016/j.jseaes.2010.08.005.

Bea, F., Montero, P., & Palma, J. F. M. (2018). Experimental evidence for the preservation of U-Pb isotope ratios in mantle-recycled crustal zircon grains. *Scientific Reports*, *8*, 12904. https://doi.org/10.1038/s41598-018-30934-4.

Berberian, M., & King, G. C. P. (1981). Towards a paleogeography and tectonic evolution of Iran. *Canadian Journal of Earth Sciences*, *18*, 210–265. https://doi.org/10.1139/e81-019.

Berra, F., & Angiolini, L. (2014). The evolution of the Tethys region throughout the Phanerozoic: A brief tectonic reconstruction. *AAPG Memoir*, *106*, 1–27. https://doi.org/10.1306/13431840M1063606.

Black, L. P., Kamo, S. L., Allen, C. M., Davis, D. W., Aleinikoff, J. N., Valley, J. W., … Foudoulis, C. (2004). Improved $^{206}Pb/^{238}U$ microprobe geochronology by the monitoring of a trace-element-related matrix effect: SHRIMP, ID-TIMS, ELA-ICP-MS and oxygen isotope documentation for a series of zircon standards. *Chemical Geology*, *205*, 115–140. https://doi.org/10.1016/j.chemgeo.2004.01.003.

Bonin, B. (2007). A-type granites and related rocks: evolution of a concept, problems and prospects. *Lithos*, *97*, 1–29. https://doi.org/10.1016/j.lithos.2006.12.007.

Boulin, J. (1991). Structures in Southwest Asia and evolution of the eastern Tethys. *Tectonophysics*, *196*, 211–268. https://doi.org/10.1016/0040-1951(91)90325-M.

Buret, Y., Quadt, A., Heinrich, C., Selby, D., Wälle, M., & Peytcheva, I. (2016). From a long-lived upper-crustal magma chamber to rapid porphyry copper emplacement: Reading the geochemistry of zircon crystals at Bajo de la Alumbrera (NW Argentina). *Earth and Planetary Science Letters*, *450*, 120–131. https://doi.org/10.1016/j.epsl.2016.06.017.

Carmichael, I. S. E. (1991). The redox states of basic and silicic magmas: A reflection of their source regions? *Contributions to Mineralogy and Petrology*, *106*, 129–141. https://doi.org/10.1007/bf00306429.

Christiansen, E. H., Haapala, I., & Hart, G. L. (2007). Are Cenozoic topaz rhyolites the erupted equivalents of Proterozoic rapakivi granites? Examples from the western United States and Finland. *Lithos*, *97*, 219–246. https://doi.org/10.1016/j.lithos.2007.01.010.

Clemens, J. D., Holloway, J. R., & White, A. R. J. (1986). Origin of A-type granite: Experimental constraints. *American Mineralogist*, *79*, 71–86.

Collins, W. J., Beams, S. D., White, A. J. R., & Chappell, B. W. (1982). Nature and origin of A-type granites with particular reference to southeastern Australia. *Contributions to Mineralogy and Petrology*, *80*, 189–200. https://doi.org/10.1007/BF00374895.

Cumming, G. L., & Richards, J. R. (1975). Ore lead isotope ratios in a continuously changing earth. *Earth and Planetary Science Letters*, *28*, 155–171. https://doi.org/10.1016/0012-821X(75)90223-X.

Dall'Agnol, R., & de Oliveira, D. C. (2007). Oxidized, magnetite-series, Rapakivi-type granites of Carajás, Brazil: Implications for classification and petrogenesis of A-type granites. *Lithos*, *9*, 215–233.

Dall'Agnol, R., Scaillet, B., & Pichavant, M. (1999). An experimental study of a Lower Proterozoic A-type granite from the Eastern Amazonian Craton, Brazil. *Journal of Petrology*, *40*, 1673–1698. https://doi.org/10.1093/petroj/40.11.1673.

Dall'Agnol, R., Teixeira, N. P., Ramo, O. T., Moura, C. A. V., Macambira, M. J. B., & de Oliveira, D. C. (2005). Petrogenesis of the Paleoproterozoic rapakivi A-type granites of the Archean Carajas metallogenic province, Brazil. *Lithos*, *80*(1–4), 101–129. https://doi.org/10.1016/j.lithos.2004.03.058.

DePaolo, D. J. (1981). Trace element and isotopic effects of combined wall rock assimilation and fractional crystallization. *Earth and Planetary Science Letters*, *53*, 189–202. https://doi.org/10.1016/0012-821X(81)90153-9.

Eby, G. N. (1990). The A-type granitoids a review of their occurrence and chemical characteristics and speculations their petrogenesis. *Lithos*, *26*, 115–134. https://doi.org/10.1016/0024-4937(90)90043-Z.

Eby, G. N. (1992). Chemical subdivision of the A-type granitoids: petrogenetic and tectonic implications. *Geology*, *20*, 641–644. https://doi.org/10.1130/0091-7613(1992)020<0641:CSOTAT>2.3.CO;2.

Eghbal, M. K., Hamzehpour, N., & Farpoor, M. H. (2018). Geology and geomorphology. In M. H. Roozitalab, H. Siadat, & A. Farshad (Eds.), *The soils of Iran* (pp. 35–56). Cham: Springer International Publishing. https://doi.org/10.1007/978-3-319-69048-3.

Fossen, H. (2010). *Structural geology* (p. 463). Cambridge: Cambridge University Press. https://doi.org/10.1017/CBO9780511777806.

Frost, B. R., Barnes, C. G., Collins, W. J., Arculus, R. J., Ellis, D. J., & Frost, C. D. (2001). A geochemical classification for granitic rocks. *Journal of Petrology*, *42*(11), 2033–2048. https://doi.org/10.1093/petrology/42.11.2033.

Frost, C. D., Frost, B. R., Chamberlain, K. R., & Edwards, B. (1999). Petrogenesis of the 1.43 Ga Sherman batholith, SE Wyoming, USA: A reduced, rapakivi-type anorogenic granite. *Journal of Petrology*, *40*, 1771–1802. https://doi.org/10.1093/petroj/40.12.1771.

Ghasemi, H., Jutea, T., Bellon, H., Sabzehei, M., Whitechurch, H., & Ricou, L. E. (2002). The mafic-ultramafic complex of Sikhoran (Central Iran): A polygenetic ophiolite complex. *Comptes Rendus Geoscience*, *334*, 431–438. https://doi.org/10.1016/S1631-0713(02)01770-4.

Golonka, J. (2004). Plate tectonic evolution of the southern margin of Eurasia in the Mesozoic and Cenozoic. *Tectonophysics*, *381*, 235–273. https://doi.org/10.1016/j.tecto.2002.06.004.

Grebennikov, A. V. (2014). A-type granites and related rocks: Petrogenesis and classification. *Russian Geology and Geophysics*, *55*, 1074–1086. https://doi.org/10.1016/j.rgg.2014.10.011.

Haapala, I., Frindt, S., & Kandara, J. (2007). Cretaceous Gross Spitzkoppe and Klein Spitzkoppe stocks in Namibia: Topaz-bearing A-type granites related to continental rifting and mantle plume. *Lithos*, *97*((1–2)), 174–192. https://doi.org/10.1016/j.lithos.2006.12.002.

Hamblin, W. K., & Christiansen, E. H. (1997). *Earth's dynamic systems* (8th ed., p. 740). New Jersey: Prentice Hall.

Hashmie, A., Rostamnejad, A., Nikbakht, F., Ghorbanie, M., Rezaie, P., & Gholamalian, H. (2016). Depositional environments and sequence stratigraphy of the Bahram Formation (middleelate Devonian) in north of Kerman, south-central Iran. *Geoscience Frontiers*, *7*, 821–834. https://doi.org/10.1016/j.gsf.2015.07.002.

Hassanzadeh, J., & Wernicke, B. P. (2016). The Neotethyan Sanandaj-Sirjan zone of Iran as an archetype for passive margin-arc transitions. *Tectonics*, *35*, 586–621.

Honarmand, M., Li, X. H., Nabatian, G., & Neubauer, F. (2017). In-situ zircon U-Pb age and Hf-O isotopic constraints on the origin of the Hasan-Robat A-type granite from Sanandaj–Sirjan zone, Iran: Implications for reworking of Cadomian arc igneous rocks. *Mineralogy and Petrology*, *111*, 659–675. https://doi.org/10.1007/s00710-016-0490-y.

Jamei, S., Ghorbani, M., Williams, I. S., & Moayyed, M. (2020). Tethyan oceans reconstructions with emphasis on the Early Carboniferous Pir-Eshagh A-type rhyolite and the Late Palaeozoic magmatism in Iran. *International Geology Review*, *63*, 1389–1405. https://doi.org/10.1080/00206814.2020.1768443.

Kearey, P., Klepeis, K. A., & Vine, F. J. (2009). *Global tectonics* (3rd ed., p. 496). Chichester UK: Wiley-Blackwell.

King, P. L., Chappell, B. W., Allen, C. A., & White, J. R. (2001). Are A-type granites the high-temperature felsic granites? Evidence from fractionated granites of the Wangrah Suite. *Australian Journal of Earth Sciences*, *48*, 501–514. https://doi.org/10.1046/j.1440-0952.2001.00881.x.

Klimm, K., Holtz, F., Johannes, W., & King, P. L. (2003). Fractionation of metaluminous A-type granites: An experimental study of the Wangrah Suite, Lachlan Fold Belt, Australia. *Precambrian Research*, *124*, 327–341. https://doi.org/10.1016/S0301-9268(03)00092-5.

Li, S., Zhao, S., Liu, X., Cao, H., Yu, S., Li, X., … Suo, Y. (2018). Closure of the Proto-Tethys Ocean and Early Paleozoic amalgamation of microcontinental blocks in East Asia. *Earth-Science Reviews*, *186*, 37–75. https://doi.org/10.1016/j.earscirev.2017.01.011.

Liu, D., Jian, P., Kroner, A., & Xu, S. (2006). Dating of prograde metamorphic events deciphered from episodic zircon growth in rocks of the Dabie–Sulu UHP complex, China. *Earth and Planetary Science Letters*, *250*, 650–666. https://doi.org/10.1016/j.epsl.2006.07.043.

Loiselle, M. C., & Wones, D. S. (1979). Characteristics and origin of anorogenic granites. *Geological Society of America*, *11*, 468.

Ludwig, K. R. (2003). *ISOPLOT 3.00: A geochronological toolkit for Microsoft Excel*. Berkeley: Berkeley Geochronology Center.

Maniar, P. D., & Piccoli, P. M. (1989). Tectonic discrimination of granitoids. *Geological Society of America Bulletin*, *101*, 635–643. https://doi.org/10.1130/0016-7606(1989)101<0635:TDOG>2.3.CO;2.

McDonough, W. F., & Sun, S. S. (1995). The composition of the Earth. *Chemical Geology*, *120*, 223–253. https://doi.org/10.1016/0009-2541(94)00140-4.

Moayyed, M., & Hosseinzade, G. (2011). Petrology and petrography of A-type Granitoids of the East-Misho Mountain with theory on its geodynamic importance. *Iranian Journal of Crystallography and Mineralogy*, *3*, 529–544.

Mohammadi, A., Moazzen, M., Lechmann, A., & Laurent, O. (2019). Zircon U-Pb geochronology and geochemistry of Late Devonian–Carboniferous granitoids in NW Iran: Implications for the opening of Paleo-Tethys. *International Geology Review*, *62*, 1931–1948. https://doi.org/10.1080/00206814.2019.1675540.

Muttoni, G., Gaetani, M., Kent, D. V., Sciunnach, D., Angiolini, L., Berra, F., … Zanchi, A. (2009). Opening of the Neo-Tethys Ocean and the Pangea B to Pangea A transformation during the Permian. *GeoArabia*, *14*, 17–48. https://doi.org/10.1016/S0012-821X(03)00452-7.

Muttoni, G., Mattei, M., Balini, M., Zanchi, A., Gaetani, M., & Berra, F. (2009). The drift history of Iran from the Ordovician to the Triassic. In M.-F. Brunet, M. Wilmsen, & J. W. Granath (Eds.), *South Caspian to Central Iran basins* (Vol. 312, pp. 7–29). London: GSL Special Publications. https://doi.org/10.1144/SP312.2.

Nabatian, G., Li, X.-H., Honarmand, M., & Esmaeili, R. (2021). The magmatic evolution of the Neotethyan rift: Geochronologic, isotopic, and geochemical evidence from A-type felsic magmatism, NW Iran. *Journal of Geodynamics*, *145*, 101829. https://doi.org/10.1016/j.jog.2021.101829.

Pearce, J. A., Bender, J. F., De-Long, S. E., Kidd, W. S. F., Low, P. J., Güner, Y., … Mitchell, J. G. (1990). Genesis of collision volcanism in eastern Anatolia. *Journal of Volcanology and Geothermal Research*, *44*, 189–229. https://doi.org/10.1016/0377-0273(90)90018-B.

Pearce, J. A., Harris, N. B. W., & Tindle, A. G. (1984). Trace element discrimination diagrams for the tectonic interpretation of granitic rocks. *Journal of Petrology*, *25*, 956–983. https://doi.org/10.1093/petrology/25.4.956.

Riel, N., Jaillard, E., Martelat, J. E., Guillot, S. E., & Braun, J. (2018). Permian-Triassic Tethyan realm reorganization: Implications for the outward Pangea margin. *Journal of South American Earth Sciences*, *81*, 78–86. https://doi.org/10.1016/j.jsames.2017.11.007.

Saccani, E., Azimzadeh, Z., Dilek, Y., & Jahangiri, A. (2013). Geochronology and petrology of the Early Carboniferous Misho Mafic Complex (NW Iran), and implications for the melt evolution of Paleo-Tethyan rifting in Western Cimmeria. *Lithos*, *162*, 264–278. https://doi.org/10.1016/j.lithos.2013.01.008.

Samperton, K. M., Schoene, B., Cottle, J. M., Keller, C. B., Crowley, J. L., & Schmitz, M. D. (2015). Magma emplacement, differentiation and cooling in the middle crust: Integrated zircon geochronological–geochemical constraints from the Bergell Intrusion, Central Alps. *Chemical Geology*, *417*, 322–340. https://doi.org/10.1016/j.chemgeo.2015.10.024.

Schoene, B., Schaltegger, U., Brack, P., Latkoczy, C., Stracke, A., & Günther, D. (2012). Rates of magma differentiation and emplacement in a ballooning pluton recorded by U–Pb TIMS-TEA, Adamello batholith, Italy. *Earth and Planetary Science Letters*, *355–356*, 162–173. https://doi.org/10.1016/j.epsl.2012.08.019.

Sengor, A. M. C. (1990). A new model for the Late Palaeozoic-Mesozoic tectonic evolution of Iran and implications for Oman. In A. H. Robertson, M. P. Searle, & A. C. Ries (Eds.), *The geology and tectonics of the Oman region* (Vol. 49, pp. 797–831). London: GSL Special Publications. https://doi.org/10.1144/GSL.SP.1992.049.01.49.

Sepehr, M., & Cosgrove, J. W. (2004). Structural framework of the Zagros Fold–Thrust Belt, Iran. *Marine and Petroleum Geology*, *21*, 829–843. https://doi.org/10.1016/j.marpetgeo.2003.07.006.

Shafaii Moghadam, H., Li, X. H., Griffin, W. L., Stern, R. J., Thomsen, T. B., Meinhold, G., … O'Reilly, S. Y. (2017). Early Paleozoic tectonic reconstruction of Iran: Tales from detrital zircon geochronology. *Lithos*, *268–271*, 87–101. https://doi.org/10.1016/j.lithos.2016.09.008.

Shafaii Moghadam, H., Li, X. H., Ling, X. X., Stern, R. J., Khedr, M. Z., Chiaradia, M., … Tamura, A. (2015b). Devonian to Permian evolution of the Paleo-Tethys Ocean: New evidence from U-Pb zircon dating and Sr-Nd-Pb isotopes of the Darrehanjir-Mashhad ophiolites, NE Iran. *Gondwana Research*, *28*, 781–799. https://doi.org/10.1016/j.gr.2014.06.009.

Shafaii Moghadam, H., Li, X. H., Ling, X. X., Stern, R. J., Santos, J. F., Meinhold, G., … Shahabi, H. (2015a). Petrogenesis and tectonic implications of Late Carboniferous A-type granites and gabbronorites in NW Iran: Geochronological and geochemical constraints. *Lithos*, *212–215*, 266–279. https://doi.org/10.1016/j.lithos.2014.11.009.

Shahzeidi, M., Moayyed, M., Murata, M., Yui, T. F., Arai, S., Chen, F., … Ahmadian, J. (2017). Late Ediacaran crustal thickening in Iran: Geochemical and isotopic constraints from the **550 Ma Mishu granitoids (Northwest Iran). *International Geology Review*, *59*, 793–811. https://doi.org/10.1080/00206814.2016.1198728.

Shakerardakani, F., Neubauer, F., Masoudi, F., Mehrabi, B., Liu, X., Dong, Y., … Friedl, G. (2015). Panafrican basement and Mesozoic gabbro in the Zagros orogenic belt in the Dorud–Azna region (nw Iran): Laser-ablation ICP–MS zircon ages and geochemistry. *Tectonophysics*, *647*, 146–171. https://doi.org/10.1016/j.tecto.2015.02.020.

Shellnutt, J. G., & Zhou, M. F. (2007). Permian peralkaline, peraluminous and metaluminous A-type granites in the Panxi district, SW China:

Their relationship to the Emeishan mantle plume. *Chemical Geology*, *243*(3–4), 286–316. https://doi.org/10.1016/j.chemgeo.2007.05.022.
Soffel, H. C., & Forster, H. G. (1980). Apparent polar wander path of Central Iran and its geotectonic Interpretation. *Journal of Geomagnetism and Geoelectricity*, *32*, 117–135. https://doi.org/10.5636/jgg.32.Supplement3_SIII117.
Stampfli, G. M. (2000). *Tethyan oceans* (Vol. 173, pp. 1–23). London: GSL Special Publications. https://doi.org/10.1144/GSL.SP.2000.173.01.01.
Stampfli, G. M., & Borel, G. D. (2002). A plate tectonic model for the Paleozoic and Mesozoic constrained by dynamic plate boundaries and restored synthetic oceanic isochrons. *Earth and Planetary Science Letters*, *196*, 17–33. https://doi.org/10.1016/S0012-821X(01)00588-X.
Stampfli, G. M., Mosar, J., Favre, P., Pillevuit, A., & Vanney, J. C. (2001). Permo Mesozoic evolution of the Western Tethys Realm: The Neotethys East Mediterranean Basin connection. *Mémoires du Muséum national d'histoire naturelle*, *186*, 51–108.
Sun, S. S., & McDonough, W. F. (1989). Chemical and isotopic systematic of oceanic basalts: Implications for mantle composition and processes. In A. S. Saunders & M. J. Norry (Eds.), *Magmatism in ocean basins* (Vol. 42, pp. 13–345). London: GSL Special Publications. https://doi.org/10.1144/GSL.SP.1989.042.01.19.
Tapster, S., Condon, D. J., Naden, J., Noble, S. R., Petterson, M. G., Roberts, N. M. W., … Smith, D. J. (2016). Rapid thermal rejuvenation of high-crystallinity magma linked to porphyry copper deposit formation; evidence from the Koloula Porphyry Prospect, Solomon Islands. *Earth and Planetary Science Letters*, *442*, 206–217. https://doi.org/10.1016/j.epsl.2016.02.046.
Taylor, S. R., & McLennan, S. M. (1985). *The continental crust: Its composition and evolution. Geoscience Texts* (p. 312). London, England: Blackwell Scientific Publications.
Topuz, G., Candan, O., Okay, A. I., von Quadt, A., Othman, M., Zack, T., & Wang, J. (2020). Silurian anorogenic basic and acidic magmatism in Northwest Turkey: Implications for the opening of the Paleo-Tethys. *Lithos*, *356*, 105302.
Topuz, G., Hegner, E., Homam, S. M., Ackerman, L., Pfänder, J. A., & Karimi, H. (2018). Geochemical and geochronological evidence for a Middle Permian oceanic plateau fragment in the Paleo-Tethyan suture zone of NE Iran. *Contributions to Mineralogy and Petrology*, *173*, 81.
Trumbull, R. B., Harris, C., Frindt, S., & Wigand, M. (2004). Oxygen and neodymium isotope evidence for source diversity in Cretaceous anorogenic granites from Namibia and implications for A-type granite genesis. *Lithos*, *73*(1–2), 21–40. https://doi.org/10.1016/j.lithos.2003.10.006.
von Raumer, J. F., Bussy, F., Schaltegger, U., Schaltegger, U., Schulz, B., & Stampfli, G. M. (2013). Pre-Mesozoic Alpine basements: Their place in the European Paleozoic framework. *Geological Society of America Bulletin*, *125*, 89–108. https://doi.org/10.1130/B30654.1.
von Raumer, J. F., & Stampfli, G. M. (2008). The birth of the Rheic Ocean – Early Palaeozoic subsidence patterns and subsequent tectonic plate scenarios. *Tectonophysics*, *461*, 9–20. https://doi.org/10.1016/j.tecto.2008.04.012.
Wang, Q., Wyman, D. A., Li, Z. X., Bao, Z. W., Zhao, Z. H., Wang, Y. X., … Chen, L. L. (2010). Petrology, geochronology and geochemistry of ca. 780 Ma A-type granites in South China: Petrogenesis and implications for crustal growth during the breakup of the supercontinent Rodinia. *Precambrian Research*, *178*, 185–208. https://doi.org/10.1016/j.precamres.2010.02.004.
Whalen, J. B., Currie, K. L., & Chappell, B. W. (1987). A-type granites: Geochemical characteristics, discrimination and petrogenesis. *Contributions to Mineralogy and Petrology*, *95*, 407–419. https://doi.org/10.1007/BF00402202.
Williams, I. S. (1998). Chapter 1, U-Th-Pb geochronology by ion microprobe. In M. A. McKibben, W. C. Shanks, III, & W. I. Ridley (Eds.), *Applications of microanalytical techniques to understanding mineralizing processes* (Vol. 7, pp. 1–35). Littleton: Reviews of Economic Geology.
Zanchetta, S., Berra, B., Zanchi, A., Bergomi, M., Caridroit, M., Nicora, A., & Heidarzadeh, G. (2013). The record of the Late Palaeozoic active margin of the Palaeotethys in NE Iran: Constraints on the Cimmerian orogeny. *Gondwana Research*, *24*, 1237–1266. https://doi.org/10.1016/j.gr.2013.02.013.
Zanchi, A., Zanchetta, S., Berra, F., Mattei, M., Garzanti, E., Molyneux, S., … Sabouri, J. (2009). The Eo-Cimmerian (Late? Triassic) orogeny in North Iran. In M.-F. Brunet, J. Wilmsen, & W. Granath (Eds.), *South Caspian to Central Iran basins* (Vol. 312, pp. 31–56). London: GSL Special Publications. https://doi.org/10.1144/SP312.3.
Ziegler, P. A., Cloetingh, S., Guiraud, R., & Stampfli, G. M. (2001). Peri-Tethyan platforms: Constraints on dynamics of rifiting and basin inversion. In P. A. Ziegler, W. Cavazza, A. H. F. Robertson, & S. Crasquin-Soleau (Eds.), *Peri-Tethyan Rift/Wrench basins and passive margins* (Vol. 6, pp. 51–108). Paris: Mémoires du Muséum National D'histoire Naturelle.

SUPPORTING INFORMATION

Additional supporting information may be found online in the Supporting Information section at the end of this article.

How to cite this article: Jamei, S., Ghorbani, M., Jafari, A., Williams, I. S., & Moayyed, M. (2021). Geochronology and tectonic significance of A-type granite from Misho, NW Iran: Implications for the detachment of Cimmeria from Gondwana and the opening of Neo-Tethys. *Geological Journal*, *56*(10), 5275–5289. https://doi.org/10.1002/gj.4236